Vortex Ring and Helical Current Formation in Superconductors Driven by a THz-Field-Induced Toroidal Vector Potential

*Björn Niedzielski and Jamal Berakdar**

Herein, the vortex dynamics in a type II superconducting torus driven by a curl-free vector potential corresponding to a toroidal moment is studied, which is triggered within picoseconds in an enclosed semiconductor by polarization-structured THz vector field pulses. Numerical simulations of the time-dependent Ginzburg–Landau equation in the presence of the toroidal vector potential evidence the formation of vortex ring structures that depend on the toroidal moment strength with a behavior resembling the Little–Parks effect. Applying in addition a static external magnetic flux density, the induced textures in the superconducting phase can be stabilized and steered to form stripe domains with corresponding helical supercurrent density.

1. Introduction

While a magnetic field is shielded by a conventional superconductor (SC), a type-II SC responds to an external magnetic field by forming vortices or fluxons.[1,2] These are localized filaments in the SC in which the supercurrent j_s swirls around a normal conducting core.[3,4] In an extended system, they interact and form a lattice. Under an electric bias fluxons may cause a finite resistance and therefore efforts are made to control their motion.[5–13] j_s, which is intimately related to variations in the phase φ_s of the SC order parameter, can also be induced by an electric bias applied to Ohmic contacts to the SC. The question of interest here is whether we can act directly and in a time-resolved way on φ_s without magnetic fields or wiring to diffusive contacts. To address this issue, we recall that within the Ginzburg–Landau formulation of SC, the free-energy density contains a Lifshitz-type invariant that is proportional to $\mathbf{T}\mathbf{v}_s \propto \sum_i T_i \partial_{\mathbf{r}_i} \varphi_s$, where $\mathbf{v}_s$ is the superfluid velocity.[14,15] $\mathbf{T}$ is an externally applied toroidal moment.[16–20] We note that it is well feasible to realize charge and current distributions that generate only $\mathbf{T}$ with the associated vector potential $\mathbf{A}_T$ being quasi-stationary and curl free, that is, no electric or magnetic fields (only $\mathbf{T}$) are radiated and felt by charges and currents. Thus, in an SC sample, only phase-sensitive carriers would respond coherently to $\mathbf{A}_T$. To achieve a time resolution on the picosecond time scale, we need to realize a correspondingly fast toroidal switch, meaning we have to be able to trigger $\mathbf{A}_T$ on a picosecond time scale, which would allow a time-resolved control on φ_s and $\mathbf{v}_s$ and can be useful for devices that functionalize φ_s.

How to generate a steady-state $\mathbf{A}_T$ within picoseconds? In a recent study,[21] it was shown that a toroidal moment can be triggered in a nanoscopic normal-state (semiconductor) torus (typical dimensions are shown in **Figure 1**a,b) upon the applications of two time-delayed THz pulses. One of the pulses is radially polarized[22] with a propagation direction piercing the torus (chosen as $\mathbf{e}_z$, cf. Figure 1b), whereas the second pulse is spatially homogeneous and linearly polarized along $\mathbf{e}_z$. The frequency of both pulses is resonant with electronic transition within the semiconductor torus. As evidenced by quantum dynamic simulations, the THz fields drive a poloidal charge current density $\mathbf{K}_T$ (marked green in Figure 1b) in the torus, meaning $\mathbf{K}_T$ has only a φ component (cf. Figure 1a). In total, the THz pulses generate a poloidal charge current I. The generated magnetic flux density $\mathbf{B}_T$ (with a corresponding magnetic flux Φ_T) is fully confined to within the semiconductor torus and vanishes outside it. Outside the torus, the curl-free (gauge invariant) vector potential $\mathbf{A}_T$ (with $\mathbf{B}_T = \nabla \times \mathbf{A}_T$) signals the existence of a toroidal moment $\mathbf{T}$ hosted by the semiconductor torus and launched by the THz irradiation;[21] typical field lines of $\mathbf{A}_T$, which we use later in the numerical SC dynamics simulations are shown by Figure 1c. The torus geometry of the semiconductor is essential to support eigenstates that carry a poloidal current. The type of excitation sketched in Figure 1b is also important to be able to excite these states resonantly from the ground state. The level space of the state involved in the THz excitation determines how fast we can switch on $\mathbf{A}_T$. From material science point of view, hybrid superconductor–semiconductor structure and devices are well feasible (as mentioned by Frasca and Charbon and Vaitiekėnas et al.[23–26] and references therein). Later, we present simulations for the response of Type-II SC to $\mathbf{A}_T$, that is, a SC for

B. Niedzielski, J. Berakdar
Institut für Physik
Martin-Luther Universität Halle-Wittenberg
06099 Halle/Saale, Germany
E-mail: jamal.berakdar@physik.uni-halle.de
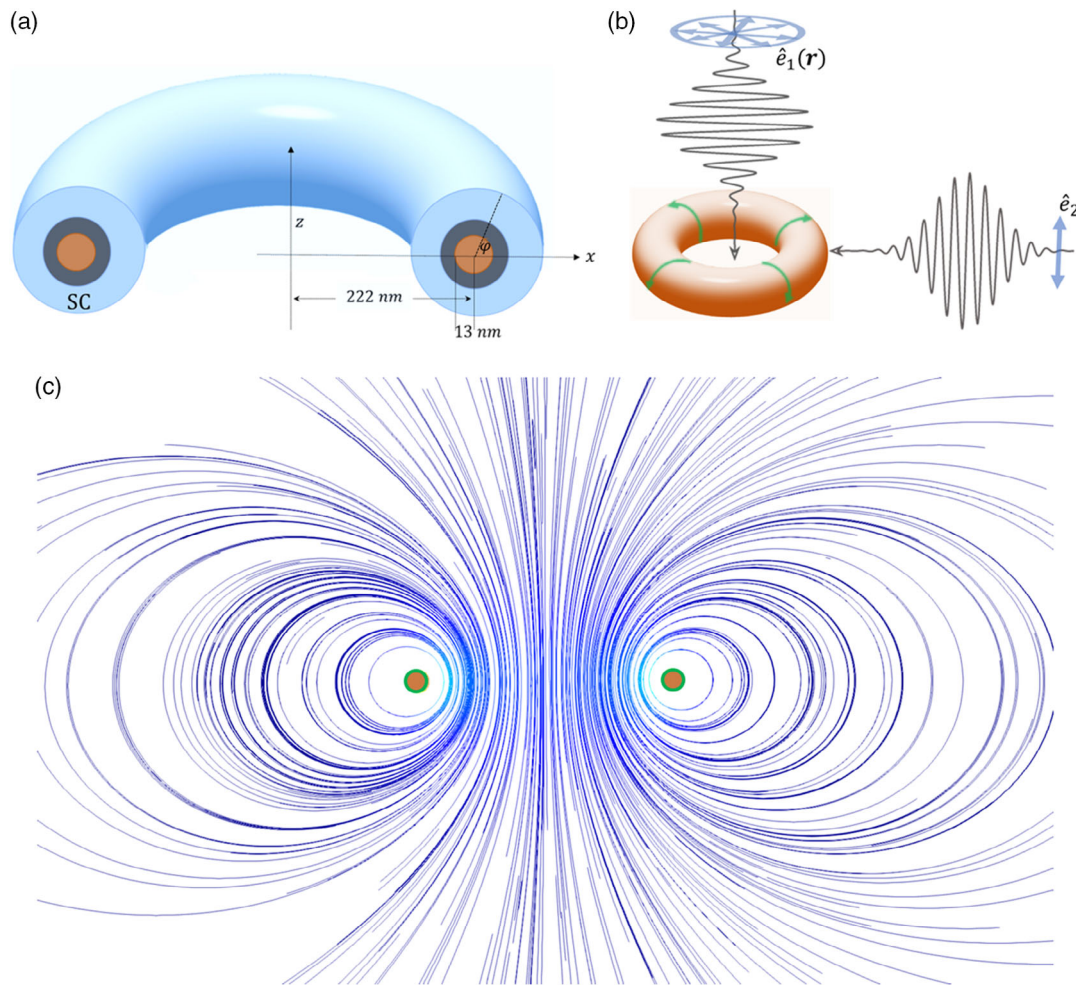
Figure 1. The considered system consists of a nanoscale semiconductor torus (orange) covered by an insulating spacer layer followed by a SC layer (not to scale). a) A cross-sectional view. b) Two crossed time-delayed THz pulses with radial polarization $\hat{e}_1$ and linear polarization $\hat{e}_2$ trigger within picoseconds resonant electronic transitions in the semiconductor ring generating a stationary poloidal charge current (green arrows).[21] The associated magnetic field is enclosed within the semiconductor. No electric or magnetic fields are generated outside the orange torus. The associated curl-free vector potential $\mathbf{A}_T$ is, however, finite due to the torus toroidal moment. c) Typical field lines in the x–z plane (orange circles indicate the positions of the orange torus). We study the SC dynamics in response to the buildup of $\mathbf{A}_T$.

which the ratio κ between the magnetic field penetration depth λ_{GL} and the coherence length of the superconducting state ξ_{GL} is larger than $1/\sqrt{2}$. The THz pulses in the frequency range discussed later have no significant direct effects on the SC parameters. The results are generic and reply on geometry, topology, the polarization, and frequency properties of the exciting fields.

2. Theoretical Modeling

For a quantification of the sketched ideas, we consider the structure shown schematically in Figure 1. The semiconductor-based torus hosting the poloidal current density (emanating the vector potential) is covered by a SC layer with a spacer layer separating the semiconducting and the SC torus. We note that the frequency of the THz fields is chosen to match transitions to states in the semiconducting torus that carry a poloidal current (generating

$\mathbf{A}_T$). The spectrum of the semiconductor is independent of the SC material parameters that determine for example the SC gap. Thus, the THz fields can be tuned such that they affect the semiconductor torus only and the toroidal moment acts on the SC. Outside the semiconductor torus, a classical charge does not experience any Lorentz force. As shown by Wätzel and Berakdar,[21] the THz-excited toroidal state is an eigenstate of the semiconductor torus, that is, it is only pumped by the THz pulse and persists in a quasi-static manner after the pulse has gone (this is due to the torus geometry). In fact, the time structure of the toroidal moment is such that it rises linearly at short times when applying the THz pulses and stabilizes at a fixed value, which persists after the pulses are over.[21] This time behavior is adopted for $\mathbf{A}_T$ in the calculations later. The strength of $\mathbf{A}_T$ is quantified by the magnetic flux enclosed within the torus Φ_T, measured in units of flux quantum $\Phi_0 = h/q_s$. The magnetic flux density associated with Φ_T is confined to within

the torus limb and after the buildup, it can be well-modeled by $\mathbf{B}_T = A_{T0}\mathbf{e}_\varphi/\rho$,[21] with $A_{T0} = \mu_0 I/2\pi$.[27] Thus, for convenience, we may write

$$\Phi_T = a\xi\mu_0 I \frac{1 - \sqrt{1-\xi^2}}{\xi^2} \tag{1}$$

where $\xi = a/b$ and $a = 13$ nm and $b = 222$ nm are the minor and major radii of the torus, respectively. We calculated the current I from the THz-driven quantum dynamics. Equation (1) follows from classical electrodynamics. For the details on how $\mathbf{A}_T$ (or Φ_T) rises in time and stabilizes and on how to control its strength via the THz pulses and for information on the semiconductor torus parameters, we refer to work by Wätzel and Berakdar,[21] to avoid repetition and concentrate here on the SC part of the study. To simulate the dynamics of the order parameter Ψ, we solve for the time-dependent Ginzburg–Landau (TDGL) equations.[28]

$$\gamma\left(\hbar\frac{\partial\Psi}{\partial t} + iq_s\phi\Psi\right) + \Psi(\beta|\Psi|^2 + \alpha) + \frac{1}{2m_s}\left(\frac{\hbar}{i}\nabla - q_s\mathbf{A}\right)^2\Psi = 0 \tag{2}$$

Here, the standard boundary condition for superconductor–insulator interfaces

$$\left(\frac{\hbar}{i}\nabla\Psi - q_s\mathbf{A}\Psi\right)\cdot\mathbf{n} = 0 \tag{3}$$

is applied, ensuring that the supercurrent has no component perpendicular to the sample boundary. The constants q_s and m_s are the charge and mass of a single Cooper pair and γ, α, and β are temperature-dependent material parameters. To simplify the solution of Equation (2), we apply the vanishing electric potential gauge $\phi = 0$ to the scalar potential.[29] From the SC order parameter Ψ, we obtain the local density of Cooper pairs $n_s = |\Psi|^2$. In our case, the wave function is normalized by its bulk value Ψ_∞. This means $n_s = 1$ corresponds to fully superconducting behavior and $n_s = 0$ signals normal conductance. In what follows, we assume $\mathbf{A} = \mathbf{A}_T$ (i.e., the toroidal-moment vector potential A_T that we use in the simulations is assumed to be much larger than the induced vector potential in SC). We note that including the vector potentials associated with the THz pulses in the calculations (or including them alone in the GL equations) leads only to fast minor variations in Ψ that average to zero. $\mathbf{A}_T$ is stabilized in time, and hence can act markedly on the SC, because the associated quantum states in the semiconductor are eigenstates.

The toroidal field $\mathbf{A}_T$ in the full space is calculated from Ampéres law

$$\frac{1}{\mu_0}\nabla\times\nabla\times\mathbf{A}_T = \nabla\times\mathbf{B}_T \tag{4}$$

with open boundary conditions, that is, $A_T \to 0$ for $r \to \infty$. The solution of Equation (4) is used as input for the first TDGL equation. From previous quantum simulations,[21] we infer that the time (t) dependence of the toroidal vector potential can be assumed as $\mathbf{A}_T = A_{T0}t$. The initial field $\mathbf{A}_{T0}$ follows Equation (4) with an initial value of $A_{T0} = 88.572$ mT nm. We neglect the interaction of the SC with its own magnetic field

$\mathbf{B}_s = \nabla\times\mathbf{A}_s$. Although, the eddy current flow and the self-field interaction can, in principle, be taken into account by solving the full set of TDGL equations.[5] In our case, setting $\mathbf{A}_s$ to zero is a reasonable approximation since the superconducting layer is much thinner than the magnetic penetration depth. When additional external magnetic fields $\mathbf{B}_e$ are applied to the SC, we write $\mathbf{A} = \mathbf{A}_T + \mathbf{A}_e$. For the external vector potential, the symmetric gauge $\mathbf{A}_e = 0.5B_e\rho\mathbf{e}_f$ is chosen, leading to the magnetic flux density $\mathbf{B}_e = B_e\mathbf{e}_z$, meaning that the field is parallel to the torus central axis. The numerical simulations are performed for Nb_3Sn with the following parameters: $\lambda_L(T=0) = 65$ nm, $\lambda_L(T = 0.9T_C) = 111$ nm, and $\kappa = 30$.[30] Thus, the SC layer thickness is well below the London penetration depth. Here, the generally accepted two-fluid model[31] for the temperature dependence of λ_L was used, where $\lambda_L(T) = \lambda_L(0)/\sqrt{1 - (T/T_c)^4}$. The diffusion constant γ is assumed to be similar to that of Nb.[10] For the numerical implementation, the system shown in Figure 1a is enclosed in a cubic box of the side length $a = 2.74$ μm. The box is necessary to approximate the open boundary conditions imposed on $\mathbf{A}_T$. A standard Galerkin finite-element (FEM)[32] method with conventional Lagrange elements for Ψ and first-order Nédelec elements for $\mathbf{A}_T$ is used and the calculations are performed with the FEM software Fenics. The Generation of the FEM mesh has been done with the software Gmsh.[33]

3. Numerical Results

3.1. Vortex Ring Formation

To investigate how the SC reacts to the current flow in the torus, we ramped up the corresponding magnetic flux Φ_T with a rate $\Delta\Phi/\Delta t = 0.312\Phi_0$/ps. For this rate of increase in the toroidal vector potential, the SC behaves non-adiabatically. This means the SC reacts transiently and cannot relax to an equilibrium state within the time in which Φ_T is almost constant. Instead, at each instance of time, the magnetic flux in the semiconducting torus is increased incrementally changing the transient state of the SC. The simulations capture the dynamic evolution of the superconducting state and the results can potentially be assessed in real experiments. The rise up of $\mathbf{A}_T$ (or Φ_T) drives a supercurrent j_s in the SC (cf. **Figure 2**) that also affects the Cooper pair density $|\Psi|^2$ (cf. **Figure 3**). Of interest here is the behavior of j_s.

The effect that $\mathbf{A}_T$ has on the SC can be understood by writing the order parameter in its amplitude-phase form $\Psi = \Psi_0(\mathbf{r}, t)e^{i\varphi_s(\mathbf{r}, t)}$. The supercurrent density can be written as a gauge-invariant phase gradient

$$\mathbf{j}_s = \frac{q_s}{m_s}\Psi_0^2(\hbar\nabla\varphi_s - q_s\mathbf{A}) = n_s q_s \mathbf{v}_s \tag{5}$$

For small fields, the order-parameter amplitude is only slightly affected and we have $\Psi_0 = 1$. For solenoidal fields, the supercurrent density increases linearly with the applied vector potential. The phase evolves such that the boundary condition Equation (3) is always fulfilled. For higher field values, the order parameter is locally suppressed and the relation between the supercurrent and field becomes nonlinear. In our case, $B_T = \nabla\times\mathbf{A}_T = 0$ in the SC
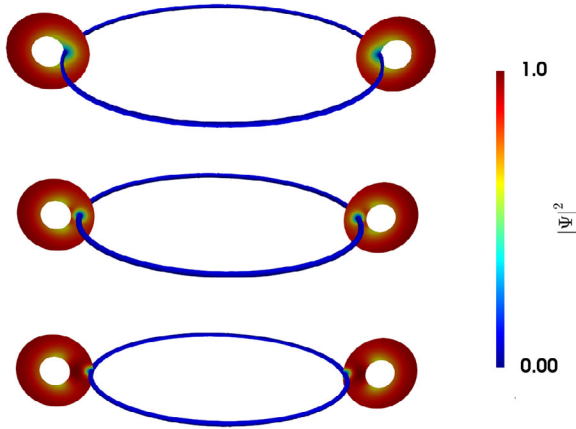
Figure 2. Typical behavior of the rise (top) and decay (middle and bottom) (within 66ps) of a vortex ring structure in the torus (shown are full vortex rings, but only the torus cross sections are depicted). The vortex rings build up in the inner region of the SC torus in proximity to the semiconductor torus. There, A_T is largest. The vortex rings wander then toward the center of the SC donut and diminish at the boundary. $\Phi_T = 3.954\Phi_0$.
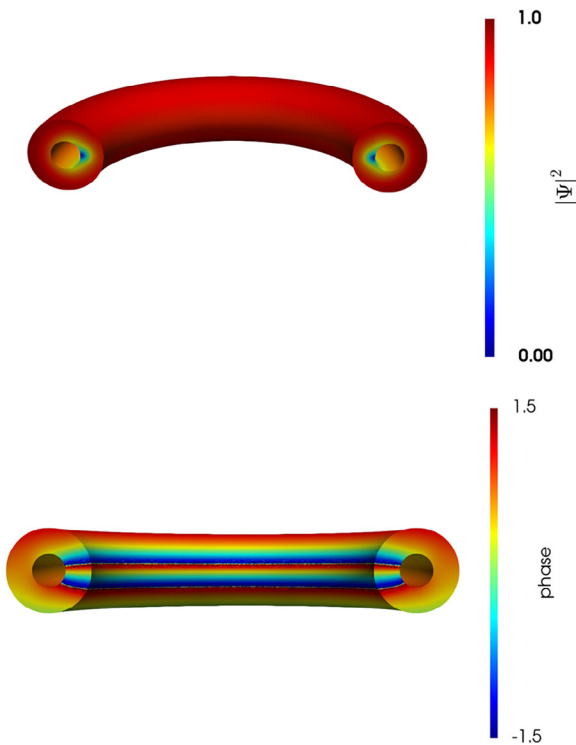
Figure 3. Superconducting density $|\Psi|^2$ (top) and its phase φ_s (bottom). In this particular case, the vortex ring is formed when the toroidal vector potential rises to a value corresponding to $\Phi_T = 3.954\Phi_0$.

and naturally one would expect $\mathbf{j}_s = 0$ since the phase and the vector potential compensate for each other. However, the field lines of $\mathbf{A}_T$ are still solenoidal and the topology dictates that $\oint_\Gamma \mathbf{A}_T \cdot d\mathbf{l} = \Phi_T$, even if $\nabla \times \mathbf{A}_T = 0$ locally. Γ here is a path which encloses the magnetic flux completely. The superconducting phase cannot compensate such a field and therefore a finite

supercurrent flows. This is only possible if there exists a path Γ in the SC, which encloses the magnetic flux Φ_T. Otherwise, the vector potential can be written as $\mathbf{A} = \nabla u$ and the earlier argument fails.[27] If we integrate Equation (5) along the path Γ which encloses the magnetic flux of the torus, we obtain the fluxoid quantization condition (see, e.g., ref. [30]):

$$\frac{m_s}{q_s} \oint_\Gamma \mathbf{v}_s = k\Phi_0 - \Phi_T, \quad k \in \mathbb{Z} \qquad (6)$$

The quantity on the left is the fluxoid taking values that are multiples of the magnetic flux quantum Φ_0. Essentially, Equation (6) is a condition for energy minimization. With an increasing amplitude of the vector potential, the superfluid velocity increases as well and the kinetic energy of the system rises. For sufficiently strong fields, the system can relax by expelling one flux quantum from its interior. In the course of this process, the phase winding number k increases by one increment. The corresponding phase jump is accompanied by the emergence of a vortex. Increasing further the strength of the toroidal moment more vortices are expelled from the SC and the energy of the system oscillates with the applied field. The behavior resembles the Little–Parks oscillations in thin-walled superconducting cylinders.[2] However, in our case, the SC has a different topology and the applied field is highly inhomogeneous in space. Therefore, the current flow due to $\mathbf{A}_T$ and the conditions for the vortex entry are changed as well, since they both depend on the geometry of the system.[34–36] We note that the vortices in our SC torus appear as closed rings. The emergence of such vortex loops is typical in systems where the field lines of the applied magnetic field form closed paths inside the SC material,[37,38] but vortex loops were also proposed to be realizable in Josephson Junctions[39] and in current-driven SCs.[40]

As the toroidal field is ramped up, $|\Psi|^2$ decreases gradually, as shown in Figure 2. When a critical value $\Phi_T = 3.954\Phi_0$ is reached, $|\Psi|^2$ admits a minimum which correlates with the formation of a vortex ring at the inner side of the SC and in the proximity to the semiconductor torus (there, A_T is largest, as seen from Figure 1c). As we do not include any pinning or external magnetic fields, the vortex ring diffuses toward the torus center along a path of decreasing A_T and eventually collapses (within $\approx$ 66ps for the simulations shown in Figure 2). The behavior of $|\Psi|^2$ indicates an SC phase jump from $-\pi/2$ to $\pi/2$. This is confirmed by Figure 3, which also shows the spatial structure of the corresponding superconducting density. The normal conducting core heals after the vortex ring diffuses and disappears. For higher critical values Φ_T, vortex rings are again formed when quantized phase jumps are met, similarly as in Figure 3.

Generally, the behavior of j_s on the external vector potential is more involved than in the case of a 2D system with a flat geometry. This is because of the SC torus topology and also due to the fact that $\mathbf{A}_T$ is inhomogeneous, as illustrated by the example in **Figure 4** and **5**. The supercurrent flows around the torus limb counteracting the external vector potential, as can be seen from Equation (5). For small fields, we have $|\Psi|^2 \approx 1$ and the maximum value of $\mathbf{j}_s$ appears at the inner side of the torus, where A_T is maximal. As the vector potential is increased, the SC density decreases and the supercurrent density is suppressed as well (see Figure 5). Prior to the emergence of the vortex ring, $|\Psi|^2$ and
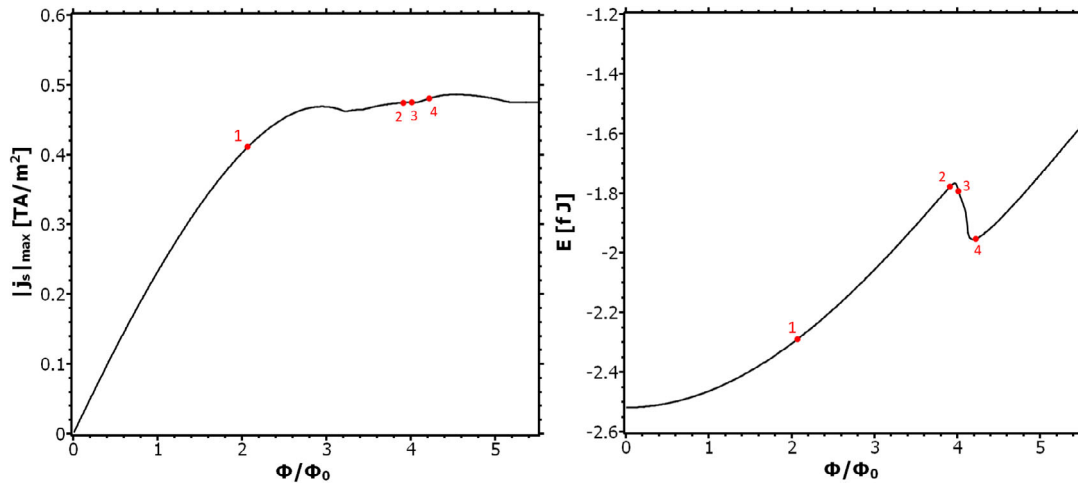
Figure 4. Left: The change in the magnitude of the supercurrent j_s with increasing strength of the toroidal vector potential and the associated magnetic flux Φ_T, which is fully enclosed within the semiconductor ring. Right: Ginzburg–Landau (GL)-free energy of the SC. The numbering corresponds to the states shown in Figure 5.
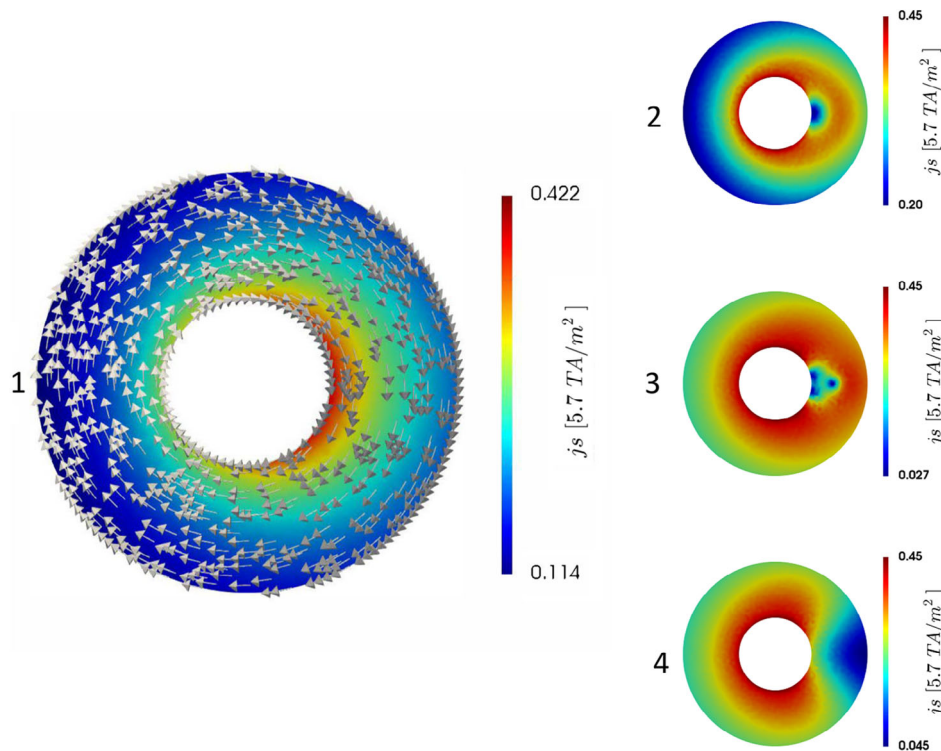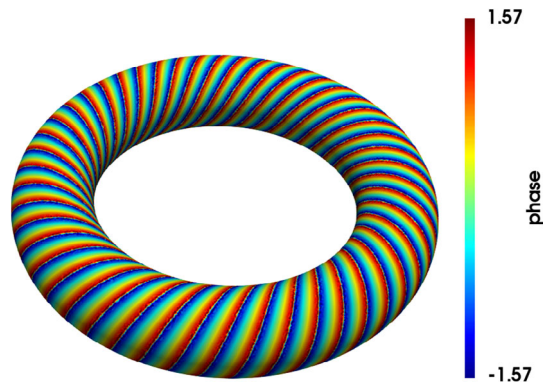

Figure 5. Left: Spatial distribution of the supercurrent density $\mathbf{j}_s$ (arrows indicate the directions) in a cross section of the torus for 1) $\Phi_T = 2.069\Phi_0$. Right: Magnitude of the supercurrent density on a slice through the torus limb for 2) $\Phi_T = 3.912\Phi_0$, 3) $\Phi_T = 4.015\Phi_0$, and 4) $\Phi_T = 4.221\Phi_0$.

$\mathbf{j}_s$ both vanish at inner side of the torus. As the vortex ring develops fully, the phase field of the vortex requires the supercurrent to flow around the normal conducting core, in a way that obeys Equation (6). After the vortex is expelled, the order parameter recovers and $\mathbf{j}_s$ flows along its original direction. However, the phase field of the vortex is still present and screens the external vector potential to some extent. The appearing vortex ring signals

the transition of the system into a state of reduced current density and lower energy (see Figure 4).

The irregular structures in $|j_s|_{\max}$, shown in Figure 4, can be partially traced to the vortex ring formation. In addition, the inhomogeneity in the SC phase and current is not restricted to the vortex region. With increasing Φ_T, the SC current becomes inhomogeneous with the largest value being where the external vector

2100622 (5 of 7)

Figure 6. Spatial distribution of the superconducting phase $\varphi_s(\mathbf{r})$ in the presence of a steady-state toroidal vector potential and an increasing external magnetic flux density $\mathbf{B}_E = B_E \mathbf{e}_z$.

potential is strongest, namely at the inner side of the torus. Here, the SC order parameter experiences the strongest suppression, which in return affects $\mathbf{j}_s$. The amplitude and the position of the supercurrent maximum may therefore change with increasing the external field strength, leading to the involved behavior in Figure 4. The suppressed density also affects the entry condition for fluxons via a modification of the corresponding energy barrier.[35,36] This is the reason why a vortex ring forms affecting locally $|\Psi|$, and why this interplay between $|\Psi|$ and j_s, while evolving in time (according to Equation (2)), results in the involved structures in Figure 4.

3.2. Helical Supercurrent

From Figure 2, it is clear that the induced vortex ring eventually diminishes in absence of external stabilization. In contrast, we expect that an external magnetic flux piercing the torus should lead to a persistent Aharonov–Bohm current j_s^θ around the torus (θ direction).[1,2] Thus, we anticipate that applying, in addition to $\mathbf{A}_T$, a magnetic flux density $\mathbf{B}_E = B_E \mathbf{e}_z$ should lead to a stable helical structure of the current and superconducting phase. The corresponding numerical results are shown in **Figure 6** for the superconducting phase. The uniqueness of phase entails the existence of a topological number counting the smooth current windings along the φ and θ directions. Recalling the relation to the supercurrent velocity and considering the localized nature of the structures in the supercurrent, we also may quantify the helical current with two components of the orbital angular momentum vector of the superconducting density. From the spatial structure of φ_s (and the associated superconducting current density), we may also infer on the formation of a finite toroidal moment in the superconducting layer. We note that superconducting toroidal moments were discussed as interesting candidates for SC-based information processing.[41]

4. Conclusions

This work presents a proposal for driving and structuring the superconducting dynamic in a torus via field-free vector potential

that can be induced by THz radiation in a nearby semiconducting structure. We performed full numerical simulations that show the formation and motion of vortex rings. The rings can be modulated to a helical-phase texture extending over the entire torus and forming a helical current by applying an additional homogeneous external magnetic flux density.

Conflict of Interest

The authors declare no conflict of interest.

Data Availability Statement

The data that support the findings of this study are available from the corresponding author upon reasonable request.

[1] J. Bardeen, M. J. Stephen, *Phys. Rev.* **1965**, *140*, A1197.
[2] M. Tinkham, *Introduction to Superconductivity*, 2nd ed., Dover Publications, Mineola, NY **2004**.
[3] E. Zeldov, A. I. Larkin, V. B. Geshkenbein, M. Konczykowski, D. Majer, B. Khaykovich, V. M. Vinokur, H. Shtrikman, *Phys. Rev. Lett.* **1994**, *73*, 1428.
[4] A. D. Hernández, D. Domínguez, *Phys. Rev. B* **2002**, *65*, 144529.
[5] F. Antončík, O. Jankovský, T. Hlásek, V. Bartůněk, *Nanomaterials* **2020**, *10*, 1429.
[6] J. I. Martín, M. Vélez, J. Nogués, I. K. Schuller, *Phys. Rev. Lett.* **1997**, *79*, 1929.
[7] V. Metlushko, U. Welp, G. W. Crabtree, Z. Zhang, S. R. J. Brueck, B. Watkins, L. E. DeLong, B. Ilic, K. Chung, P. J. Hesketh, *Phys. Rev. B* **1991**, *59*, 603.
[8] L. Civale, A. D. Marwick, T. K. Worthington, M. A. Kirk, J. R. Thompson, L. Krusin-Elbaum, Y. Sun, J. R. Clem, F. Holtzberg, *Phys. Rev. Lett.* **1991**, *67*, 648.
[9] O. Daldini, P. Martinoli, J. L. Olsen, G. Berner, *Phys. Rev. Lett.* **1974**, *32*, 218.
[10] B. Niedzielski, J. Berakdar, *Phys. Status Solidi* **2020**, *257*, 1900709.
[11] B. Niedzielski, C. L. Jia, J. Berakdar, *Nanomaterials* **2021**, *11*, 184.
[12] C. González-Ruano, D. Caso, L. G. Johnsen, C. Tiusan, M. Hehn, N. Banerjee, J. Linder, F. G. Aliev, *Sci. Rep.* **2021**, *11*, 19041.
[13] A. Lara, F. G. Aliev, A. V. Silhanek, V. V. Moshchalkov, *Sci. Rep.* **2015**, *5*, 9187.
[14] A. I. Buzdin, *Phys. Rev. Lett.* **2008**, *101*, 107005.

[15] V. M. Edelstein, *J. Phys.: Condes. Matter* **1996**, *8*, 339.

[16] I. B. Zel'Dovich, *Sov. Phys. JETP* **1958**, *6*, 1184.

[17] G. Afanasiev, V. Dubovik, *Phys. Part. Nucl.* **1998**, *29*, 891.

[18] A. Boardman, K. Marinov, N. Zheludev, V. Fedotov, *Phys. Rev. E* **2005**, *72*, 036603.

[19] J. S. T. Gongora, A. E. Miroshnichenko, Y. S. Kivshar, A. Fratalocchi, *Nat. Commun.* **2017**, *8*, 15535.

[20] G. Afanasiev, *J. Phys. D: Appl. Phys.* **2001**, *34*, 539.

[21] J. Wätzel, J. Berakdar, *Adv. Quantum Technol.* **2019**, *2*, 1800096.

[22] Q. Zhan, *Adv. Opt. Photonics* **2009**, *1*, 1.

[23] S. Frasca, E. Charbon, *Nat Electron* **2019**, *2*, 433.

[24] P. Krogstrup, N. L. B. Ziino, W. Chang, S. M. Albrecht, M. H. Madsen, E. Johnson, J. Nygård, C. M. Marcus, T. S. Jespersen, *Nat. Mater.* **2015**, *14*, 400.

[25] G. Scappucci, C. Kloeffel, F. A. Zwanenburg, D. Loss, M. Myronov, J.-J. Zhang, S. De Franceschi, G. Katsaros, M. Veldhorst, *Nat. Rev. Mater.* **2021**, *6*, 926.

[26] S. Vaitiekėnas, Y. Liu, P. Krogstrup, C. M. Marcus, *Nat. Phys.* **2021**, *17*, 43.

[27] N. J. Carron, *Am. J. Phys.* **1995**, *63*, 717.

[28] A. Schmid, *Phys. der Kondensierten Mater.* **1966**, *5*, 302.

[29] H. Kaper, J. Fleckinger-Pellé, *J. Appl. Math. Mech.* **1996**, *76* 305.

[30] R. Gross, A. Marx, *Festkörperphysik*, 2. ed., De Gruyter Oldenbourg, Berlin/Boston **2014**.

[31] a) C. J. Gorter, H. B. G. Casimir, *Phys. Z.* **1934**, *35*, 963; b) C. J. Gorter, H. Casimir, *Physica* **1934**, *1*, 306.

[32] H. Gao, W. Sun, *J. Comput. Phys.* **2015**, *294*, 329.

[33] M. S. Alnaes, J. Blechta, J. Hake, A. Johansson, B. Kehlet, A. Logg, C. Richardson, J. Ring, M. E. Rognes, G. N. Wells, *Arch. Numer. Softw.* **2015**, *3*, 9.

[34] C. P. Bean, J. D. Livingston, *Phys. Rev. Lett.* **1964**, *12*, 14.

[35] E. Zeldov, A. I. Larkin, V. B. Geshkenbein, M. Konczykowski, D. Majer, B. Khaykovich, V. M. Vinokur, H. Shtrikman, *Phys. Rev. Lett.* **1994**, *73*, 1428.

[36] A. D. Hernández, D. Domínguez, *Phys. Rev. B* **2002**, *65*, 144529.

[37] M. M. Doria, A. R. de C. Romaguera, M. V. Miloševik, F. M. Peeters, *EPL* **2007**, *79*, 47006.

[38] G. R. Berdiyorov, M. M. Doria, A. R. de C. Romaguera, M. V. Milošević, E. H. Brand, F. M. Peeters, *Phys. Rev. B* **2013**, *87*, 184508.

[39] G. R. Berdiyorov, M. V. Milošević, F. Kusmartsev, F. M. Peeters, S. Savel'ev, *Sci. Rep.* **2018**, *8*, 2733.

[40] E. H. Fyhn, J. Linder, *Phys. Rev. B* **2019**, *100*, 214503.

[41] A. M. Zagoskin, A. Chipouline, E. Chipouline, J. R. Johansson, F. Nori, *Sci. Rep.* **2015**, *5*, 16934.